Volume xx (200y), Number z, pp. 1–12

Stress Constrained Thickness Optimization for Shell Object Fabrication

Haiming Zhao[1], Weiwei Xu [†1], Kun Zhou[1], Yin Yang[2], Xiaogang Jin[1] and Hongzhi Wu[1]

[1]State Key Lab of CAD&CG, Zhejiang University, China
[2]Electrical and Computer Engineering Department, The University of New Mexico, USA

Abstract

We present an approach to fabricate shell objects with thickness parameters, which are computed to maintain the user-specified structural stability. Given a boundary surface and user-specified external forces, we optimize the thickness parameters according to stress constraints to extrude the surface. Our approach mainly consists of two technical components: First, we develop a patch-based shell simulation technique to efficiently support the static simulation of extruded shell objects using finite element methods. Second, we analytically compute the derivative of stress required in the sensitivity analysis technique to turn the optimization into a sequential linear programming problem. Experimental results demonstrate that our approach can optimize the thickness parameters for arbitrary surfaces in a few minutes and well predict the physical properties, such as the deformation and stress of the fabricated object.

Categories and Subject Descriptors (according to ACM CCS): I.3.3 [Computer Graphics]: Three-Dimensional Graphics and Realism—Geometry

1. Introduction

3D printing is an additive manufacturing technique to physically realize a 3D object from its digital design. The rapid development of desktop 3D printers makes it affordable and easy-to-use for home users, to turn their creative geometry design into reality.

To fabricate a desired object, the user needs to create a 3D geometry first, typically using commercial modeling software (e.g., Maya and 3DS Max). Such a geometry is usually represented by its boundary surface, which is infinitely thin and cannot be directly printed. To tackle this issue, most 3D printing software either converts the design into a solid object, or extrudes the original boundary surface based on certain thickness parameters, to produce a printable object with an inner hollow volume (which we denote as *shell objects*). For geometries with non-closed surfaces, converting to solid objects is not an ideal option, as all original holes will be closed (as illustrated in Fig. 1). Printing solid objects is also material- and time-consuming. Therefore, users resort to shell objects for fabrication in many applications.

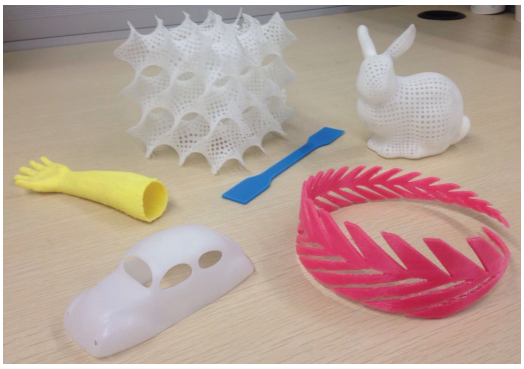

Figure 1: *Examples of shell objects.*

One grand challenge in fabricating shell objects is to guarantee satisfactory structural stabilities of fabricated objects. Recently, researchers have proposed various approaches to improve the structural strengths, including adding inner struts [SVB*12], or embedding frame structures, while sav-

† weiwei.xu.g@gmail.com

ing the printing and support material cost [WWY*13]. For geometries with non-closed surfaces, adding support structures, however, would make the fabricated objects differ from their original designs either visually or functionally. The added support structures can be partially seen or affect how the objects are used.

In this paper, we introduce an approach to fabricate shell objects with optimized thickness parameters, which are computed to maintain the user-specified structural stability without additional support structures. Specifically, we aim to minimize the shell thickness so that the stress at each vertex of the input surface under given external forces is below the required maximum strength of the designated material. Thus, the finite element method (FEM) is integrated to simulate the static equilibrium of shell objects and compute the stress values. We adopt the triangular shell element in simulation due to that it already incorporates the shell thickness as a parameter in the strain-stress relationship, which significantly facilitates the derivative computation in the optimization.

The main technical challenge is that the extrusion of surface according to prescribed thickness values is not a simple geometric operation, since it might lead to self-intersections for concave or thin regions where their thickness parameters should be carefully determined. To avoid self-intersections, we can allow each vertex of the surface to have its own thickness parameter and set up its limits in the optimization. However, such problem setting requires a large number of thickness variables in the optimization. Moreover, due to the local nature of the stress, the maximal stress constraints need to be formulated at each vertex, resulting in a large number of nonlinear inequality constraints. These two issues make the entire optimization unstable and significantly slow.

We develop an efficient algorithm to compute thickness parameters with stress constraints to handle the above technical challenges. It is made possible with three novel features:

- We segment an input surface into a number of patches, and each patch is assigned with a single thickness parameter to significantly reduce the optimization variables. However, observing that the regions of high stress values are usually concave, our algorithm chooses to keep full thickness optimization degrees-of-freedoms (DOFs) for concave regions. We adopt the fuzzy cut method [Kat03] to segment the surface and extract such regions. Since the method prefers to cut the surface at concave edges, the patches obtained are mainly convex. Thus, the patch boundaries need to be enlarged to include concave regions. Figure 2 illustrates such a segmentation result on a bunny model, where the concave regions are extracted and covered by so-called transitional regions. Each vertex inside transitional regions is assigned an individual thickness parameter to fully allow the deformation and thickness optimization DOFs. Transitional regions also enable a smooth thickness transition between patches. The maximal thickness values for surface extrusion without self-intersections are computed by the extended distance field algorithm in [PKZ04].
- We adopt the sensitivity analysis technique to compute the derivative of stress with respect to thickness parameters, and convert the original nonlinear optimization problem into sequential linear programming problems. To facilitate the sensitivity analysis technique based on the static equilibrium equation constructed for shell objects, a closed-form solution to compute the derivative of stiffness matrix with respect to the thickness parameters is also derived.
- We develop an alternating optimization algorithm (AOP) to optimize patch and transitional region thickness respectively to avoid the numerical instability problem in optimization.

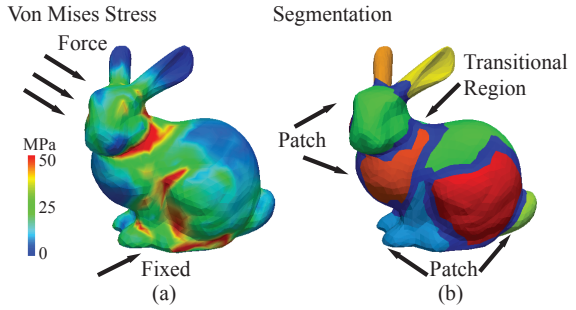

Figure 2: *A segmentation result on bunny model. (a) is the von Mises stress result under the external force applied on the head and the bottom is fixed. (b) is the segmentation result. Note the regions with high stress value (indicated in red) are usually concave and covered by the transitional regions. We allow maximal deformation and thickness optimization DOFs at such regions.*

Experimental results demonstrate that our approach can optimize the thickness parameters for arbitrary surfaces in a few minutes and well predict the physical properties, such as the deformation and stress of the fabricated object.

2. Related Work

Stress-based structure optimization in practical engineering optimizes the shape of a structure for a minimal stress. Comprehensive surveys on the topic can be found in [Din86, SINP05]. Shape optimization integrated with FEM analysis was pioneered by Zienkiewicz and Campbell [ZC73] using sequential linear programming. To avoid the oversized number of non-linear inequalities constraints on stress, global stress measure functions are adopted, such as p-norm, p-mean and Kreisselmeier-Steinhauser (KS) function [YC96, AFB12]. Big p or large penalty coefficients are used to control the peak stress or stress concentration in global measure based methods. In the optimization with respect to stress constraints, the shapes can be parameterized

using splines or other linear combinations of basis functions [BF84], or can be parameterization-free by solving for FEM node positions directly. In the latter case, surface smoothness regularization terms are required to obtain high-quality results [BFLW10, AFB12]. The level-set method was also applied to shape and topology optimization [Xia12]. The FEM analysis integrated in these methods are usually based on tetrahedral meshes. In contrast, our choice of shell element directly takes the thickness as a parameter in stress computation (see Appendix B for details), which facilitates the computation of derivatives required in the optimization algorithm. Although the shell object can also be modeled by thin tetrahedrons, the number of degrees of freedom in shell simulation is less than tetrahedral mesh, since the original surface needs to be grown on both sides and two vertices need to be generated for one vertex in the case of thin tetrahedrons. The reduction of deformation DOFs is also beneficial to our optimization algorithm.

Our work is related to the sensitivity analysis technique in [PNCC10, AFB12]. The technique has also been recently applied to cloth simulation to fast predict how clothing deformation changes according to the change of the clothing design parameters [UKIG11, XUC*14]. Derivatives of the stiffness matrix with respect to the model parameters have been explored in [BBO*09, BBO*10]. In our paper, we derive an analytic formula to compute the derivatives of stiffness entries with respect to thickness parameters.

3D printing receives a significant amount of research interests recently. Computer-aided design algorithms, in conjunction with simulation techniques, have been developed to control the physical properties of 3D printable objects, such as deformation [BBO*10, STC*13], articulation [CCA*12, BBJP12], mechanical motion [ZXS*12, CTN*13, CLM*13] and appearance [DWP*10, LDPT13, CLD*13].

The goal of structural stability analysis of the 3D printable design is to detect structurally weak regions and improve its strengths through the shape optimization. To satisfy the stress constraints, Stava *et al.* [SVB*12] developed stress relief operations, such as hollowing and thickening; Zhou *et al.* [ZPZ13] proposed a fast linear element-based method to analyze the worst load distribution. Domain decomposition method has also been applied to locally update the FEM entities to fast predict the influence of shape editing to the structural stability [XXY*15]. In comparison, our algorithm optimizes the thickness of digital thin shell objects in their 3D printed counterparts.

Our work is also inspired by partitioning a 3D model into parts to facilitate its 3D printing. Luo *et al.* [LBRM12] proposed to segment a large model into small parts so that the parts can be fabricated in the printing volume of a 3D printer. The structural soundness is also an important criteria in their segmentation algorithm. In [VGB*14], the surface of an object to be printed is divided into small shell parts so as to save supporting materials and printing time. A reduced order optimization framework is developed in [MAB*15] to optimize the generation of offset surfaces with varying thickness to improve the mass distribution and static stability of 3D objects. A recent contribution in [HLZCO14] introduced approximate pyramidal shape decomposition to decompose a volume into pyramidal shape which is optimal for fabrication. However, the structural stability is not considered in their algorithm.

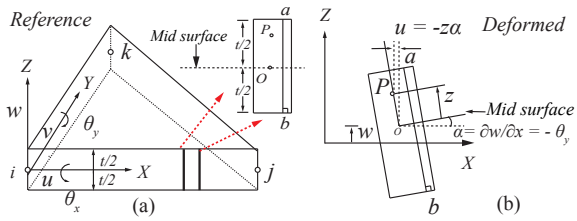

Figure 3: *A shell element. (a) A triangular shell element. (b) Plate bending deformation demonstrated using a small rectangle cut off from X direction (shown in (a) with red arrows).*

Shell simulation is widely used in computer graphics to simulate deformation behaviors of thin shell objects, such as hat, paper and cloth. The deformation energy of thin shell usually consists of membrane and flexural energies. Cirak *et al.* [COS00] proposed a shell representation of subdivision surfaces, and computed the shell deformation energies according to the local coordinate system formed in the subdivision. Grinspun *et al.* [GHDS03] used the change of dihedral angle at each edge in a two-manifold mesh as the flexural energy, and achieved realistic simulation results for shell objects with curved un-deformed configuration. The modal analysis technique has also been applied to achieve real-time simulation [CYWK07].

Thin shell objects can also be efficiently simulated using 3D point clouds [WSG05]. Gu *et al.* [GLB*06] formulated the shell deformation energy based on a global conformal parameterization of point cloud surfaces. Their method supports the simulation of fracturing effects. The elaston model developed in [MKB*10] significantly extends the meshless simulation method in [MHTG05], which unifies the simulation of solids, shells and beams.

3. Computational Model

The goal of computational model is to set up the static equilibrium equation of shell objects to calculate the nodal displacements using FEM. Shell elements and linear elasticity with the isotropic material model are adopted to simulate the deformation behavior and then obtain the stress distributions for shell objects [Log11].

Shell element: We adopt the Kirchhoff Plate Bending (KPB) model and the total potential energy method (TPE) [Fel13] in order to speed up calculating the derivatives

of stiffness matrix. The KPB model is base on Kirchhoff-Love theory of plates, assuming that the thickness of a plate remains constant during its deformation [Wik16]. The basic geometry of a shell element is shown in Fig. 3. Its thickness t is much less than its other dimensions, and the strain along its local Z direction is ignored in shell deformation according to Kirchhoff-Love theory. In our implementation, the shell element is the combination of Kirchhoff plate bending element and plane stress element.

As illustrated in Fig. 3, one node in the mid-surface of a triangular shell element embodies 5 DOFs $\{u, v, w, \theta_x, \theta_y\}$. The first two DOFs $\{u, v\}$ represent the displacements of the nodes on the mid-surface, which is the local XY plane of a shell element. This defines the plane stress element, to model the on-plane stretch deformation. The Cauchy strain for such stretch deformation can be simply written as:

$$\varepsilon_x = \frac{\partial u}{\partial x}, \quad \varepsilon_y = \frac{\partial v}{\partial y}, \quad \varepsilon_{xy} = \frac{1}{2}(\frac{\partial u}{\partial y} + \frac{\partial v}{\partial x}). \tag{1}$$

The remaining three DOFs $\{w, \theta_x, \theta_y\}$ represent the plate bending, where w denotes the displacement of shell along the Z direction. The following formula holds:

$$\frac{\partial w}{\partial x} = -\theta_y, \qquad \frac{\partial w}{\partial y} = \theta_x. \tag{2}$$

Therefore, given $\{w, \theta_x, \theta_y\}$ at each node, a curved mid-surface is interpolated to model the bending behavior of a shell. With the deformation DOFs, the components of Cauchy strain tensor of plate bending can be written as [Log11]:

$$\varepsilon_x = -z\frac{\partial^2 w}{\partial x^2}, \quad \varepsilon_y = -z\frac{\partial^2 w}{\partial y^2}, \quad \varepsilon_{xy} = -2z\frac{\partial^2 w}{\partial x \partial y}. \tag{3}$$

Note that ε_z is assumed to be 0.

The sub-block of the element stiffness matrix corresponding to one vertex of a triangular element $\mathbf{K}_{ele}$ in its local coordinate system has the following form derived using virtual work theory as [Fel13]:

$$\mathbf{K}_{ele} = \begin{pmatrix} \mathbf{K}_{stre} & 0 & 0 \\ 0 & \mathbf{K}_{bend} & 0 \\ 0 & 0 & 0 \end{pmatrix}, \tag{4}$$

where $\mathbf{K}_{stre}$ corresponds to the plane stress part, which is of size 2×2. The plate bending part $\mathbf{K}_{bend}$ is of size 3×3. The packed row and column of 0 expand the size of element stiffness matrix 6×6 so that the stiffness matrix can be transformed to the global coordinate system. The plane stress part is determined by the $\{u, v\}$ DOFs at each vertex, and it is calculated by linear element using first-order barycentric coordinate as shape functions. The details of the computation of $\mathbf{K}_{bend}$ are described in the Appendix.

Finally, by transforming each element stiffness matrix into a global coordinate system, all local element stiffness matrices can be assembled to obtain a global stiffness matrix for static equilibrium simulation. More details are described in [Fel13].

4. Algorithm

Our algorithm starts with segmenting an input surface into a set of patches, denoted by $\mathcal{B}_S$. We then perform region growing along the boundaries of patches to form the transitional regions, which are denoted as $\mathcal{B}_T$. The set of $\mathcal{B}_T$ is for smooth thickness transition of patches and full deformation and thickness optimization DOFs of their covered concave regions. The triangles inside each patch are grouped and will be simulated using shell elements with a unified thickness. Essentially the shape of the object is determined by two set of thickness parameters: α, defining the thickness of each patch $(\alpha_1, ..., \alpha_{n_s})$ in $\mathcal{B}_S$ and, β defining the thickness of each vertex $(\beta_1, ..., \beta_{n_t})$ in $\mathcal{B}_T$. The final set of thickness parameters, α, β , are optimized with respect to user-specified external forces and stress constraints. We denote an input surface as $\mathcal{M} = \{\mathcal{V}, \mathcal{E}\}$, where $\{\mathcal{V} = \mathbf{v}_i, i = 1, ..., n\}$ is the set of vertices on the surface, and $\{\mathcal{E} = \mathbf{e}_i, i = 1, ..., m\}$ is the set of edges connecting the vertices. Our algorithm searches for the lightest parameters that are able to sustain the external force while the fabricated object remains visually pleasant. The input surface is extruded towards its outer and inner sides simultaneously with the half of the optimized thickness parameters to form the final shell object to be fabricated.

4.1. Thickness Parameters Determination

There are mainly two steps in thickness parameter determination: Initial surface segmentation, and thickness parameters assignment, as shown in Fig. 4.

Initial surface segmentation: We use the fuzzy cut method in [Kat03] to partition an input surface into a number of patches. The algorithm favors segmentation boundaries at concavities. Since concavities usually indicate the separation of two continuous patches, it can approximate the good continuity principle in perceptual grouping [Psy13]. The user is also allowed to improve the segmentation manually. The segmentation step allows us to use different thicknesses at different parts of the surface (i.e., to allocate more materials at critical regions).

Thickness parameters assignment: Since the difference in thickness parameters at different patches will result in discontinuities in the extruded surface, the transitional region is needed to connect neighboring patches. We thus grow the patch boundary by merging the triangles adjacent to the patch boundary edges to form transitional regions, which also covers concave regions of the input surface. After transitional region detection, we assign thickness parameters in each region. The patch thickness parameters are defined as $\{\alpha_0, ..., \alpha_{n_s}\}$. It helps to remain the specific shape of the patches and reduces the DOFs in optimization process. While in transitional regions, the thickness for each node is

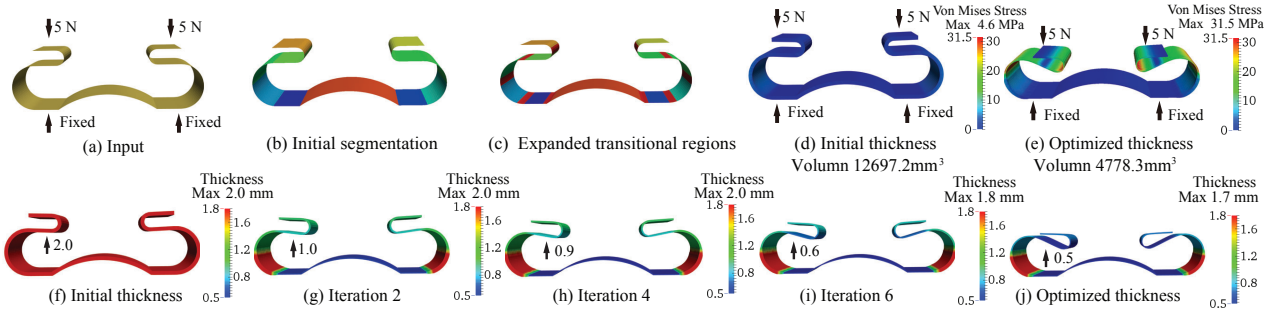

Figure 4: *Algorithm flowchart demonstrated using a table model. We optimize the input surface in (a) to obtain the extruded surface as shown in (j), by setting the upper bound of von Mises stress to 31.5 MPa. Based on segmentation information as shown in (b), we expand the boundary between segmentations and get transitional regions in red color in (c). The initial thickness parameter is set to 2.0mm (f). After iterations applied (g-i), the final result is generated (j). The von Mises stress before and after the optimization are shown in (d) and (e). The optimization results are shown with their deformations under applied external forces. The decreasing optimized thickness values of the same patch on the left wing of the model are labeled on (f-j).*

necessary to generate a smooth enough extruding surface. Therefore, the node thickness parameters are represented as $\{\beta_0, ..., \beta_{n_t}\}$.

Note that we use an individual thickness parameter for each vertex in transitional regions. However, in the shell element model, each triangular shell element possesses a single thickness. We thus treat the triangle thickness as the average of its three vertex thickness parameters. Using node thickness as optimization variables is more straightforward in the formulation of our problem as shown in next section. Thus, the number of thickness parameters in our algorithm can be counted as $n_s + n_t$, where n_s is the number of patches and n_t is the number of nodes in transitional regions.

4.2. Thickness Optimization

The goal of thickness optimization is to minimize a set of thickness parameters so that its maximum stress under designated external forces is within the specified strength limit. By minimizing the thickness parameters, considerable printing time and material cost for shell objects can be saved, while its stress is still within the safe threshold.

Problem setting: Suppose that we have partitioned an input surface into patch regions, the objective function of the thickness optimization can then be written as:

$$\begin{aligned} \min_{\mathbf{U}_T, \mathbf{U}_S, t_i} \quad & \left\| \begin{bmatrix} \mathbf{K}_T & 0 \\ 0 & \mathbf{K}_S \end{bmatrix} \begin{bmatrix} \mathbf{U}_T \\ \mathbf{U}_S \end{bmatrix} - \mathbf{F} \right\|^2 + \sum_{i=1}^{n} t_i s_i \\ \text{s.t.} \quad & \sigma_v(\mathbf{U}_T, \mathbf{U}_S) < \sigma_{max}, \quad \forall v \in \mathcal{V}, \\ & t^{min} < t_i < t_i^{max}, \quad i = 1..n, \\ & -\zeta < t_i - \sum_{j \in adj(i)} \lambda_j t_j < \zeta, \end{aligned} \tag{5}$$

where t_i represents the thickness for both patch regions and the nodes in transitional regions, and s_i the region areas. For vertices on triangles in transitional regions, its area is approximated by one third of the sum of the areas of the triangles incident to this vertex. The vertex displacements at both regions are represented by vector $\mathbf{U}_S$ for nodes in patch regions and $\mathbf{U}_T$ for transitional regions. The first term in the objective function is designed to minimize the residual force at the static equilibrium. The second term is used to minimize the printing volume, which is approximated by the product of the thickness parameters with the corresponding areas. t^{min} is determined by the minimal thickness available for 3D printing.

The first inequality constraint says that the von Mises stress σ_v at each vertex v is required to be lower than a user-specified maximum stress threshold σ_{max}, which is usually set as the strength limit of the material used in 3D printing. In the theory of continuum mechanics [GS08], the stress state at any point p in a body is defined by a second order Cauchy stress tensor, denoted by $\{\sigma_{ij}, i = 1, ..., 3, j = 1, ..., 3\}$. However, it is difficult to directly formulate stress constraints using the stress tensor for the reason that the tensile strength for a material is a scalar to measure the uniaxial stress load asserted in mechanical tests. One successful way is to measure whether the maximal principal stress at a vertex reaches the strength limit. However, the computation of principal stress requires the eigen-decomposition of the stress tensor for which it is hard to obtain an analytical formulation.

We thus use von Mises stress in our system, which is a scalar deduced from the Cauchy stress tensor [Log11]:

$$\begin{aligned} \sigma_v^2 &= \frac{1}{2}[(\sigma_{11} - \sigma_{22})^2 + (\sigma_{22} - \sigma_{33})^2 \\ &\quad + (\sigma_{33} - \sigma_{11})^2 + 6(\sigma_{12}^2 + \sigma_{23}^2 + \sigma_{31}^2)] \\ &= (\tilde{\sigma}_1 - \tilde{\sigma}_2)^2 + (\tilde{\sigma}_2 - \tilde{\sigma}_3)^2 + (\tilde{\sigma}_3 - \tilde{\sigma}_1)^2 \end{aligned} \tag{6}$$

where $\tilde{\sigma}_1, \tilde{\sigma}_2, \tilde{\sigma}_3$ are three principal stresses, i.e. eigenvalues of a stress tensor. It can be verified that the von Mises

stress is equivalent to the maximal principal stress under the situation of uniaxial stress loading. von Mises stress can also be viewed as a conservative measurement with negative biaxial stress ratio in fracture mechanics, i.e. when the two largest principal stresses are of different signs [SJ11]. We further relate the Cauchy stress tensor with the displacements variables [Log11]. For instance, the following formula holds for σ_{11}:

$$\sigma_{11} = \frac{E}{(1+\nu)(1-2\nu)}[(1-\nu)\frac{\partial u}{\partial x} + \nu(\frac{\partial v}{\partial y} + \frac{\partial w}{\partial z})], \quad (7)$$

where $\{u, v, w\}$ are the displacements along XYZ directions. For a shell element, we ignore $\frac{\partial w}{\partial z}$, since it is assumed to 0.

The last constraint on thickness parameters is used to control the variation of thickness parameters in adjacent regions to guarantee the smoothness of the extruded surface, where λ_j is set to be the cotangent weight, which is widely used in mesh smoothing algorithms [DMSB99]. We use a small positive ζ to relax the surface smoothness constraints, to increase the flexibility of the optimization algorithm. Note that the surface smoothness constraints are only defined at the vertices of transitional triangles, since each vertex has its own thickness parameter. This constraint does not need to be defined at the vertices inside patches, as we grow each patch using the same thickness parameter.

The main challenge to optimize Eq. 5 is that it is a highly nonlinear, non-convex problem. First, the entries of stiffness matrices $\mathbf{K}_T$ and $\mathbf{K}_S$ are nonlinear functions of the thickness parameters. Altering the thickness at the rest shape requires the re-computation of stiffness matrices. Second, the inequality specified at each vertex to constrain its stress is nonlinear with respect to thickness and displacement variables due to the nonlinear nature of von Mises stress with respect to σ_{ij}.

Initial value: For shell objects, their thickness should be small compared to their area according to the assumption of the shell deformation model. We first initialize a constant thickness value for a shell object as $t^d = 0.05 r_d$ as the largest thickness for all patches and vertices, where r_d is the length of the bounding box diagonal for the model, and then adopt the extended distance field method in [PKZ04] to compute the allowable thickness t^p for each vertex in the simulation. The maximal thickness value for a vertex is finally set to be $t^{max} = \min\{t^d, t^p\}$.

In [PKZ04], the offset surface of the original surface is grown by integrating the movement according to the gradient field of the extended distance field, where the self-intersections are avoided since the gradient will gradually deviate from surface normal and will be close to zero only in areas at the concave regions. For a point at on a concave region, for example, H as shown in the right inset, the field line deviates from the normal of the surface n_H. Therefore, t^p is obtained once θ_d reaches 10° so that the formed offset surface is close to the normal direction to approximate the geometric assumption in shell simulation. For the point G located on a convex region, the extended distance is close to Euclidian distance near the surface, and its gradient at G is still equivalent to normal, as shown by the dash lines of G. In this case, the value of t^p can be set as t^d. If self-intersections still occur at the offset surface with the computed thickness values, our algorithm reduces the maximal allowable thickness to be $0.9 * t^d$ and restart the thickness computation procedure.

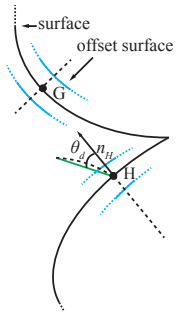

The thickness for a triangle used in shell simulation is set to be the average of the thickness values of its three vertices, and the largest thickness value for a patch is set to be the minimal largest thickness parameter of the vertices in the patch region. The initial thickness parameter values (t^i) are set to be $t^i = t^{max} * 0.8$ in optimization to start from a feasible point. We found that our thickness computation procedure can lead to accurate deformation and stress results for the generated shell objects in all our experiments.

4.3. Optimization algorithm

To handle the large number of nonlinear inequality constraints, we locally linearize the optimization problem in Eq. 5 with the sensitivity analysis technique, and solve it with sequential linear programming [ZC73, Van01]. Suppose we have obtained the thickness parameters t_i^k at iteration k in the optimization, the linear programming problem at iteration k can be formulated as:

$$\begin{aligned} \min_{\Delta t_i^k} \quad & \sum_{i=1}^{n} (t_i^k + \Delta t_i^k) s_i \\ \textbf{s.t.} \quad & \sigma_v^k + \frac{\partial \sigma_v}{\partial t}(t_i^k)\Delta t_i^k < \sigma_{max}, \quad \forall v \in M, \\ & t^{min} < t_i^k + \Delta t_i^k < t_i^{max}, \quad i = 1..n, \\ & -\zeta < (t_i^k + \Delta t_i^k) - \sum_{j \in adj(i)} \lambda_j (t_j^k + \Delta t_j^k) < \zeta. \end{aligned} \quad (8)$$

The static equilibrium constraint is absorbed into the derivative of $\frac{\partial \sigma_v}{\partial t}(t_i^k)$, using the sensitivity analysis technique [AFB12]. Specifically, we first simplify the static equilibrium for the whole system as follows:

$$\mathbf{K}_{sys}\mathbf{U} = \mathbf{F}, \quad (9)$$

where the original system stiffness matrix is denoted as $\mathbf{K}_{sys}$, and the displacement for each node is represented as $\mathbf{U}$. The sensitivity analysis technique requires the derivatives to thickness parameters t_i on its both sides:

$$\frac{\partial \mathbf{F}}{\partial t_i} = \frac{\partial \mathbf{K}_{sys}}{\partial t_i}\mathbf{U} + \mathbf{K}_{sys}\frac{\partial \mathbf{U}}{\partial t_i}. \quad (10)$$

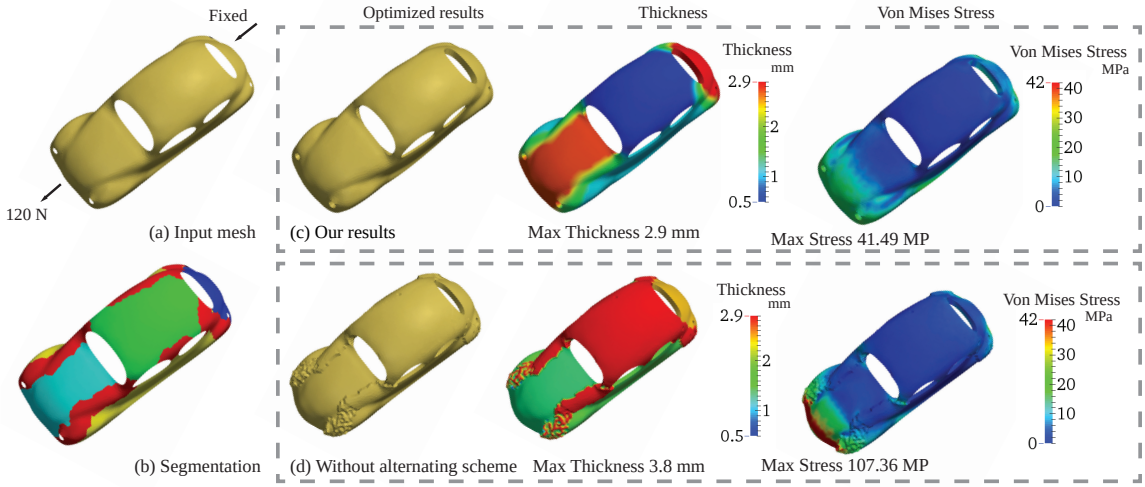

Figure 5: *Examples of multiple thickness parameters optimization with and without alternating optimization procedure. This car model is made of SLA. A 120 N external force is applied to its front while the back of the car is fixed. (a) The original input surface. (b) The patches. The transitional regions are in red. (c) Our optimization result using alternating optimization procedure. The middle and right column show the distribution of thickness and von Mises stress values of our result. (d) The jaggy optimization result without alternating scheme.*

Since external force is constant, its derivative to thickness parameter t_i is 0. Therefore, we have:

$$\frac{\partial \mathbf{U}}{\partial t_i} = -\mathbf{K}_{sys}^{-1} \frac{\partial \mathbf{K}_{sys}}{\partial t_i} \mathbf{U}. \tag{11}$$

Given the current thickness parameters t_i^k and the computed displacements $\mathbf{U}^k$ at iteration k, we can compute the derivative of displacements with respect to t_i using Eq. 11. The derivative $\frac{\partial \sigma_v}{\partial t}(t_i^k)$ is finally computed using Eq. 6 with the chain rule. The derivation of $\frac{\partial \mathbf{K}_{sys}}{\partial t_i}$ is described in the appendix.

Alternating optimization procedure: Since the vertex-level thickness parameters only affect its local neighborhood, the derivatives of stress and surface volume to them are much less than those for patch-level thickness parameters which affect whole patch regions. Taking the car model in Fig. 5 as an example, the L2 norm of stress change caused by patch thickness is 10^4 times bigger than the changes caused by a node in the transitional region, which results in a significant difference in derivative magnitude. Such magnitude differences influence the condition number of constraint matrix from the stress constraints. It will lead to numerical instability in the linear programming and the algorithm fails to converge in high probability. To overcome this issue, we optimize the set of patch thickness parameters α and transitional node thickness parameters β iteratively in two phases. These two phases are alternatively performed until convergence.

In Phase 1, we optimize α. Thus, the optimization problem (Eq. 5) is set as:

$$\begin{aligned} \min_{\Delta\alpha_i^k} \quad & \sum_{i=1}^{n} (\alpha_i^k + \Delta\alpha_i^k) s_i \\ \textbf{s.t.} \quad & \sigma_v^k + \frac{\partial \sigma_v}{\partial t}(t_i^k)\Delta t_i^k < \sigma_{max}, \quad \forall v \in \mathcal{M}, \\ & t^{min} < \alpha_i^k + \Delta\alpha_i^k < \alpha_i^{max}, \quad i = 1..n_s. \end{aligned} \tag{12}$$

In Phase 2, after the patch thicknesses are determined in Phase 1, the initial thickness for nodes in transitional regions are calculated by solving the Laplacian equation [YZX*04]. The patch thickness values are set as its boundary condition. The optimization problem is set as:

$$\begin{aligned} \min_{\Delta\beta_i^k} \quad & \sum_{i=1}^{n} (\beta_i^k + \Delta\beta_i^k) s_i \\ \textbf{s.t.} \quad & \sigma_v^k + \frac{\partial \sigma_v}{\partial t}(t_i^k)\Delta t_i^k < \sigma_{max}, \quad \forall v \in \mathcal{M}, \\ & t^{min} < \beta_i^k + \Delta\beta_i^k < \beta_i^{max}, \quad i = 1..n_t, \\ & -\zeta < (\beta_i^k + \Delta\beta_i^k) - \sum_{j \in adj(i)} \lambda_j (\beta_j^k + \Delta\beta_j^k) < \zeta. \end{aligned} \tag{13}$$

The thickness parameters for patch regions α, are calculated in Phase 1. The thickness for nodes in transitional regions β are calculated only in phase 2. To improve the prediction accuracy of the linearized stress constraints, we restrict the thickness parameters can only be optimized in an interval near their current values in each iteration. The range is set to be half the maximal thickness value at each vertex in the first iteration and gradually reduced to its one-tenth in the iterations afterwards.

5. Experimental Results

We have implemented our algorithm on a desktop PC with an Intel I7 CPU and 16G memory. We use the primal-dual simplex method in GLPK library (http://www.gnu.org/software/glpk) to solve the linear programming problem and Eigen library (http://eigen.tuxfamily.org) for stiffness matrix factorization. The material parameters used in the simulation are listed in Table 1. The algorithm statistics are listed in Table 2. In mechanical tests of the printed 3D objects, a spring scale is used to roughly measure the asserted external forces, whose unit is set to be Kilogram (Kg). In Table 2, the 3D printing technologies used to fabricate the models in the experiments are also listed. The two columns IV and OV in Table 2 are the initialized and optimized volume of the models to show how our algorithm can be applied to save materials in fabrication.

Material	E	Poisson's Ratio	Maximal stress
ABS plastics	3e9	0.35	31.5 MPa
Nylon	1.65e9	0.35	42 MPa
SLA	2.5e9	0.41	42 MPa

Table 1: *Material parameters used in the simulation. E stands for Young's Modulus.*

Physical validation: We first validate our shell simulation model by comparing the deformation between a real object and the simulation result for a bracelet model extruded with 2 mm thickness, as shown in Fig. 6. The real bracelet object is printed using ABS plastic material with the fused decomposition modeling (FDM) technique. The simulation parameter of this model is set to be Young's Modulus 3.0e9 MPa and Poisson's ratio 0.35, to match the material used in the 3D printing. Fig. 6 shows that the deformed shapes are visually close: The distance between the two ends of the bracelet model after the deformation are almost identical.

Second, the improvement of the structural stability using our optimization algorithm is demonstrated using an example of a swirl object, as shown in Fig. 9. The optimized swirl object (printed using Nylon and its optimized thickness is 1.2 mm) can support the gravitational force of an average male adult (60 Kg), while the un-optimized swirl object (thickness 0.6mm initially specified by the user) fabricated

Model	Material	Scale (mm)	IV	OV
bracelet	abs	123*43*116	29357.4	12363.3
table	abs	136*88*42	12697.2	4778.3
car	sla	98*40*34	24322.1	10231.0
arm	abs	125*57*24	12127.1	10204.1
swirl	nylon	100*100*100	11039.7	5094.3
bunny	sla	100*88*65	139963.0	19066.3

Table 2: *Statistics of the examples used in our optimization algorithm. IV stands for the initial volume and OV stands for the optimized volume in our results. The ratio of the saved volume ranges from 40% to 85%.*

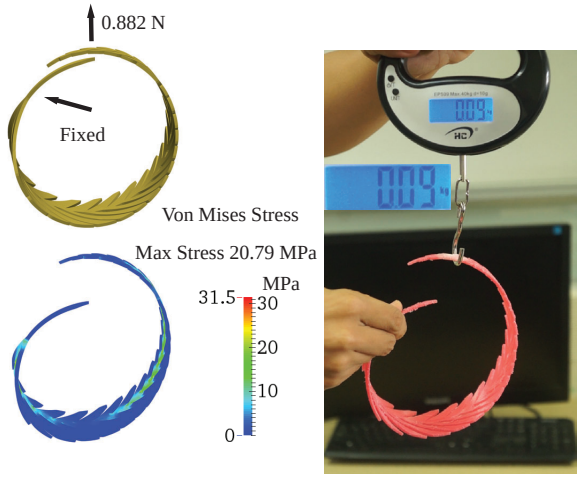

Figure 6: *Deformation comparison. The simulation parameter for the bracelet model is set to be Young's Modulus* 3.0e9 *MPa, and Poisson's ratio 0.35 to match the ABS plastic material used in 3D printing. Top left: the reference model. Bottom left: simulation result. Right: the deformation result of the printed bracelet model.*

using Nylon material is crashed under the same load. Fig. 7 illustrates the optimization with different thickness parameters at different regions. The bunny model is partitioned into 10 regions, and the external force is set to be 40 N at the left ear of the bunny model. The initial thickness parameter is set to be 9.0 mm. After the optimization, the thickness of the left ear is reduced to 1.8 mm so that the max stress is below the user-specified maximal stress value 42 MPa. In the mechanical test, it can be seen that the left ear is still stable under an external force around 4.13 Kg (which is equivalent to 40.474 N). Please also see the accompanying video for this experiment. Another two multi-thickness parameter optimization results are shown in Figs. 5 and 8.

Time evaluation: The time statistics of the proposed algorithm is listed in Table 3. It shows that the time complexity of assigning individual thickness parameter at each vertex of input surface is much slower than our patch-based optimization algorithm. For large models, optimization without segmentation is even impossible since the iteration is too slow in the evaluation of the derivatives and values of stress constraints to obtain the convergence in a reasonable time. In contrast, our algorithm can produce high-quality results for large models as shown in Fig. 5.

Convergence: Fig. 10 illustrates the convergence of max von Mises stress value and the shell volume using the alternating optimization algorithm using the car model in Fig. 5. Since the linear approximation of stress function used in the linear programming, the real stress value might exceed the maximum strength and the shell volume might occasionally rise too, even though the linearized version of stress constraints are satisfied. As the optimization progresses, the lin-

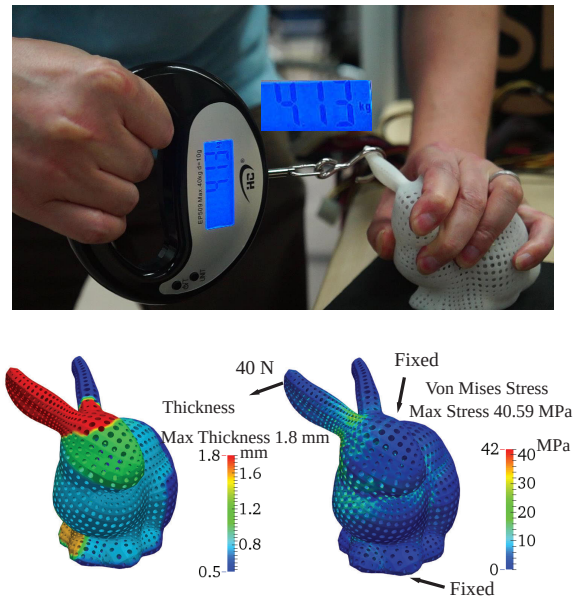

Figure 7: *Examples of multiple thickness parameters optimization. The initial thickness is set to be 9 mm, and a 40 N external force is applied to the left ear of the bunny model. Since the ears are in different regions in the thickness parameter determination stage, the thickness of the left ear is optimized to be 1.8 mm to resist the external force. The maximal stress value to be 42 MPa in the optimization. The picture on the top shows the left ear of the printed object is structurally stable under the external force 4.13 Kg, equivalent to 40.474 N.*

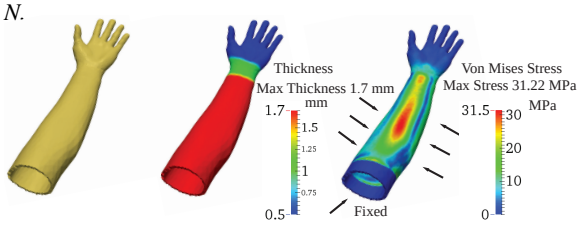

Figure 8: *Examples of multiple thickness parameters optimization. This arm model is made of ABS. The initial thickness is set to be 1.8 mm, and a 50 MPa pressure applied to the entire arm region (the hand region is pressure free). The maximal stress value to be 31.5 MPa after optimization. Left: the optimized result. Middle: the thickness distributions. Right: the von Mises stress distribution. The max thickness, 1.7 mm is gained around the max stress region(31.2 MPa).*

ear approximation is continuously corrected and the algorithm converges to optimal thickness values. The von Mises stress tends to rise in the beginning and finally converges to a value below 40 MPa, the maximal strength for SLA material. As an comparison, the optimization without AOP fails to converge to optimal value due to the numerical instability problem. In the experiment, the GLPK package continues to report numeral instability issue in the optimization procedure. The surface vibration can be noticed (Fig. 5d) to show the unpleasant optimization result without AOP.

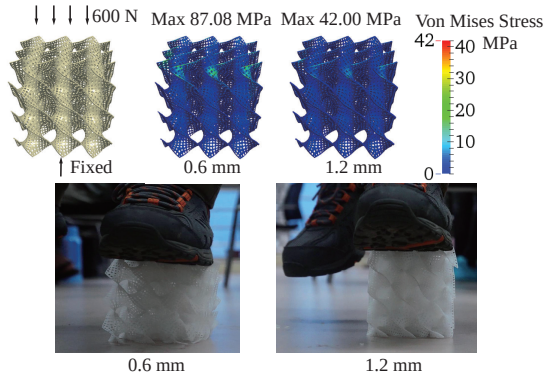

Figure 9: *Examples of structural stability optimization. The initial thickness is set to be 0.6 mm and the maximal allowed stress value 42 MPa. To simulate the support of the gravitational load of an adult of 60 Kg, a 600 N load is asserted on the upper surface of this model. The optimized model can support the gravitational load well, while the un-optimized model starts to crash (its maximum stress is 87.08MPa under the same loads, which exceeds the material strength limit). Please see the accompanying video for the detailed results.*

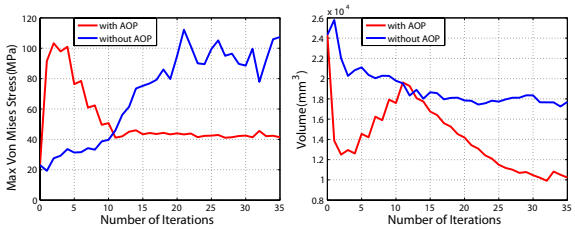

Figure 10: *Results of alternating optimization procedure (AOP) compared with optimization without AOP. The optimized shells are shown in Fig. 5. The blue lines stand for the optimization procedure without using AOP, while the red lines represent the optimization procedure using AOP.*

6. Limitations and Discussion

Our system assumes the external force is known in the structural stability optimization. However, in practice, the distribution of external force is difficult to be known in advance, except for some specific designs. One possible improvement is to apply worst-case structural analysis [ZPZ13] and try to improve the structural stability there with our optimization algorithm. The optimal thickness parameters should be related to the segmentation result. Currently, we segment the mesh using concavity measure in fuzzy cut. Although our shell simulation can be viewed as a reduced model and it is still performed on the whole mesh so that the stress constraints can be well satisfied, it is hard to guarantee the optimization result is globally optimal only using a single segmentation result. It is valuable to perform structural analysis

	With Segmentation							Without Segmentation			
Model	#Tri	#Node	Patch	Opt Node	Iteration	TPI (s)	Time (s)	DOFs	Iteration	TPI (s)	Time (s)
bracelet	6,360	3,961	1	0	3	0.63	1.9	6,360	9	1497.21	13474.9
table	12,768	6,641	11	1,455	8	1.14	9.12	12,768	NA	12465.50	NA
car	13,817	7,190	5	1,443	36	2.93	105.81	13,817	NA	10227.70	NA
arm	19,105	38,087	3	784	9	15.39	138.47	19,105	NA	NA	NA
swirl	115,205	72,839	1	0	15	85.10	1276.51	115,205	NA	NA	NA
bunny	255,343	139,827	10	14,122	19	284.56	5406.63	255,343	NA	NA	NA

Table 3: *Comparison of the optimization algorithm with and without segmentation. Patch indicates the number of patches derived from segmentation, and opt node represents the number of nodes in transitional regions, where each node is assigned with an individual thickness parameter in the optimization process. TPI is short for time per iteration, and timings are measured in seconds. For optimization process without segmentation, the DOFs represent the degree of freedom in optimization process. If the process is extremely slow and not convergent, the time consumed is tagged as NA.*

and integrate the analysis result into the segmentation algorithm as in [LBRM12].

Our approach can optimize the thickness parameters for arbitrary surfaces. However, for highly concave regions, such as sharp concavities, the allowable thickness computed by the extended distance function [PKZ04] is probably limited and not enough for a feasible solution. In this case, we pre-process the input mesh using method proposed in [DMSB99] to smooth the shape of the highly concave region to enable larger thickness there. The change is kept small so that the overall shape of the input surface is still maintained.

7. Conclusion

We have described a thickness optimization algorithm to generate shell objects with user-specified stress properties. The advantage of our method is that it can design structurally stable shell objects without additional inner struts or frames. Our algorithm turns the optimization problem with nonlinear stress constraints into a sequential linear programming problem, which can be efficiently solved even for surfaces with more than hundred thousands of FEM nodes.

In the future, we plan to investigate how to apply the sensitivity analysis technique to various 3D printing applications, especially when static equilibrium simulation is required. We now use linear elasticity and isotropic material models in shell object simulations. It is also interesting to explore how to apply anisotropic material models to further improve the FEM analysis accuracy.

8. Acknowledgements

We would like to thank the anonymous reviewers for their valuable suggestions. Weiwei Xu is partially supported by the NSFC (No. 61272392, 61322204). Kun Zhou is supported in part by the NSFC (No. 61272305). Yin Yang is supported in part by the National Science Foundation (CRII-1464306, CNS-1637092), UNM RAC & OVPR research. Xiaogang Jin is supported by NSFC (No. 61472351). Hongzhi Wu is partially supported by NSFC (No. 61303135).

References

[AFB12] ARNOUT S., FIRL M., BLETZINGER K.-U.: Parameter free shape and thickness optimisation considering stress response. *Structural and Multidisciplinary Optimization 45*, 6 (2012), 801–814. 2, 3, 6

[BBJP12] BÄCHER M., BICKEL B., JAMES D. L., PFISTER H.: Fabricating articulated characters from skinned meshes. *ACM Trans. Graph. 31*, 4 (2012), 47:1–47:9. 3

[BBO*09] BICKEL B., BÄCHER M., OTADUY M. A., MATUSIK W., PFISTER H., GROSS M.: Capture and modeling of nonlinear heterogeneous soft tissue. *ACM Transactions on Graphics (TOG) 28*, 3 (2009), 89. 3

[BBO*10] BICKEL B., BÄCHER M., OTADUY M. A., LEE H. R., PFISTER H., GROSS M., MATUSIK W.: Design and fabrication of materials with desired deformation behavior. *ACM Trans. Graph. 29*, 4 (2010), 63:1–63:10. 3

[BF84] BRAIBANT V., FLEURY C.: Shape optimal design using b-splines. *Computer Methods in Applied Mechanics and Engineering 44*, 3 (1984), 247 – 267. 3

[BFLW10] BLETZINGER K., FIRL M., LINHARD J., WŹCHNER R.: Optimal shapes of mechanically motivated surfaces. *Computer Methods in Applied Mechanics and Engineering 199*, 58 (2010), 324–333. 3

[CCA*12] CALÌ J., CALIAN D. A., AMATI C., KLEINBERGER R., STEED A., KAUTZ J., WEYRICH T.: 3d-printing of non-assembly, articulated models. *ACM Trans. Graph. 31*, 6 (2012), 130:1–130:8. 3

[CLD*13] CHEN D., LEVIN D. I. W., DIDYK P., SITTHI-AMORN P., MATUSIK W.: Spec2fab: A reducer-tuner model for translating specifications to 3d prints. *ACM Trans. Graph. 32*, 4 (2013), 135:1–135:10. 3

[CLM*13] CEYLAN D., LI W., MITRA N. J., AGRAWALA M., PAULY M.: Designing and fabricating mechanical automata from mocap sequences. *ACM Trans. Graph. 32*, 6 (2013), 186:1–186:11. 3

[COS00] CIRAK F., ORTIZ M., SCHROER P.: Subdivision surfaces: a new paradigm for thin-shell finite-element analysis. *International Journal for Numerical Methods in Engineering 47*, 12 (2000), 2039–2072. 3

[CTN*13] COROS S., THOMASZEWSKI B., NORIS G., SUEDA S., FORBERG M., SUMNER R. W., MATUSIK W., BICKEL B.: Computational design of mechanical characters. *ACM Trans. Graph. 32*, 4 (2013), 83:1–83:12. 3

[CYWK07] CHOI M. G., YONG WOO S., KO H.-S.: Real-time simulation of thin shells. *Computer Graphics Forum 26*, 3 (2007), 349–354. 3

[Din86] DING Y.: Shape optimization of structures: a literature survey. *Computers & Structures 24*, 6 (1986), 985–1004. 2

[DMSB99] DESBRUN M., MEYER M., SCHRÖDER P., BARR A. H.: Implicit fairing of irregular meshes using diffusion and curvature flow. In *Proceedings of the 26th Annual Conference on Computer Graphics and Interactive Techniques* (1999), SIGGRAPH '99, pp. 317–324. 6, 10

[DWP*10] DONG Y., WANG J., PELLACINI F., TONG X., GUO B.: Fabricating spatially-varying subsurface scattering. *ACM Trans. Graph. 29*, 4 (2010), 62:1–62:10. 3

[Fel13] FELIPPAB C.: Advanced Finite Element Methods http://www.colorado.edu/engineering/CAS/courses.d/AFEM.d/. 3, 4

[GHDS03] GRINSPUN E., HIRANI A. N., DESBRUN M., SCHRÖDER P.: Discrete shells. In *Proceedings of the 2003 ACM SIGGRAPH/Eurographics Symposium on Computer Animation* (2003), SCA'03, pp. 62–67. 3

[GLB*06] GUO X., LI X., BAO Y., GU X., QIN H.: Meshless thin-shell simulation based on global conformal parameterization. *Visualization and Computer Graphics, IEEE Transactions on 12*, 3 (May 2006), 375–385. 3

[GS08] GONZALEZ O., STUART A. M.: *A First Course in Continuum Mechanics*. Cambridge University Press, 2008. 5

[HLZCO14] HU R., LI H., ZHANG H., COHEN-OR D.: Approximate pyramidal shape decomposition. *ACM Transactions on Graphics, (Proc. of SIGGRAPH Asia 2014) 33*, 6 (2014), 213:1–12. 3

[Kat03] KATZ S.: Hierarchical mesh decomposition using fuzzy clustering and cuts. *ACM Transactions on Graphics (SIGGRAPH'03) 22*, 3 (2003), 954–961. 2, 4

[LBRM12] LUO L., BARAN I., RUSINKIEWICZ S., MATUSIK W.: Chopper: Partitioning models into 3D-printable parts. *ACM Transactions on Graphics (Proc. SIGGRAPH Asia) 31*, 6 (Dec. 2012). 3, 10

[LDPT13] LAN Y., DONG Y., PELLACINI F., TONG X.: Bi-scale appearance fabrication. *ACM Trans. Graph. 32*, 4 (2013), 145:1–145:12. 3

[Log11] LOGAN D. L.: A first course in the finite element method (fifth edition)., 2011. 3, 4, 5, 6, 12

[MAB*15] MUSIALSKI P., AUZINGER T., BIRSAK M., WIMMER M., KOBBELT L.: Reduced-order shape optimization using offset surfaces. *ACM Trans. Graph. 34*, 4 (July 2015), 102:1–102:9. 3

[MHTG05] MÜLLER M., HEIDELBERGER B., TESCHNER M., GROSS M.: Meshless deformations based on shape matching. *ACM Trans. Graph. 24*, 3 (2005), 471–478. 3

[MKB*10] MARTIN S., KAUFMANN P., BOTSCH M., GRINSPUN E., GROSS M.: Unified simulation of elastic rods, shells, and solids. *ACM Trans. Graph. 29*, 4 (2010), 39:1–39:10. 3

[PKZ04] PENG J., KRISTJANSSON D., ZORIN D.: Interactive modeling of topologically complex geometric detail. *ACM Trans. Graphics. 23*, 3 (2004), 635–643. 2, 6, 10

[PNCC10] PARIS J., NAVARRINA F., COLOMINAS I., CASTELEIRO M.: Stress constraints sensitivity analysis in structural topology optimization. *Computer Methods in Applied Mechanics and Engineering 199*, 33-36 (2010), 2110 – 2122. 3

[Psy13] PSYCHLOPEDIA: Gestalt Law http://psychlopedia.wikispaces.com/Gestalt+Laws+of+Perceptual+Grouping. 4

[SINP05] SAITOU K., IZUI K., NISHIWAKI S., PAPALAMBROS P.: A survey of structural optimization in mechanical product development. *Journal of Computing and Information Science in Engineering 5*, 3 (2005), 214–226. 2

[SJ11] SUN C.-T., JIN Z.: *Fracture Mechanics*. Elsvier, 2011. 6

[STC*13] SKOURAS M., THOMASZEWSKI B., COROS S., BICKEL B., GROSS M.: Computational design of actuated deformable characters. *ACM Trans. Graph. 32*, 4 (2013), 82:1–82:10. 3

[SVB*12] STAVA O., VANEK J., BENES B., CARR N., MĚCH R.: Stress relief: Improving structural strength of 3d printable objects. *ACM Trans. Graph. 31*, 4 (2012), 48:1–48:11. 1, 3

[UKIG11] UMENTANI N., KAUFMANN D. M., IGARASHI T., GRINSPUN E.: Sensitive couture for interactive garment modeling and editing. *ACM Transactions on Graphics 30*, 4 (2011), 90:1–9. 3

[Van01] VANDERBEI R. J.: Linear programming. *Foundations and Extensions. Second Edition-International Series in Operations Research and Management Science 37* (2001). 6

[VGB*14] VANEK J., GALICIA J. A. G., BENES B., MECH R., CARR N., STAVA O., MILLER G. S.: Packmerger: A 3d print volume optimizer. *Computer Graphics Forum 33*, 6 (2014). 3

[Wik16] WIKIPEDIA: KirchhoffĺclOve plate theory — wikipedia, the free encyclopedia, 2016. "[Online; accessed 29-April-2016]". URL: https://en.wikipedia.org/w/index.php?title=Kirchhoff-Love_plate_theory&oldid=711301274. 4

[WSG05] WICKE M., STEINEMANN D., GROSS M.: Efficient animation of point-sampled thin shells. *Computer Graphics Forum 24*, 3 (2005), 667–676. 3

[WWY*13] WANG W., WANG T. Y., YANG Z., LIU L., TONG X., TONG W., DENG J., CHEN F., LIU X.: Cost-effective printing of 3d objects with skin-frame structures. *ACM Trans. Graph. 32*, 6 (2013), 177:1–177:10. 2

[Xia12] A level set solution to the stress-based structural shape and topology optimization. *Computers & Structures 90-91*, 0 (2012), 55 – 64. 3

[XUC*14] XU W., UMENTANI N., CHAO Q., MAO J., JIN X., TONG X.: Sensitivity-optimized rigging for example-based real-time clothing synthesis. *ACM Transactions on Graphics 33*, 4 (2014), 107:1–9. 3

[XXY*15] XIE Y., XU W., YANG Y., GUO X., ZHOU K.: Agile structural analysis for fabrication-aware shape editing. *Computer Aided Geometric Design 35?6*, 0 (2015), 163 – 179. Geometric Modeling and Processing 2015. 3

[YC96] YANG R., CHEN C.: Stress-based topology optimization. *Structural optimization 12*, 2-3 (1996), 98–105. 2

[YZX*04] YU Y., ZHOU K., XU D., SHI X., BAO H., GUO B., SHUM H.-Y.: Mesh editing with poisson-based gradient field manipulation. *ACM Trans. Graph. 23*, 3 (Aug. 2004), 644–651. 7

[ZC73] ZIENKIEWICZ O., CAMPELL J.: Shape optimization and sequential linear programming. Wiley, 1973. 2, 6

[ZPZ13] ZHOU Q., PANETTA J., ZORIN D.: Worst-case structural analysis. *ACM Trans. Graph. 32*, 4 (2013), 137:1–137:12. 3, 9

[ZTZ08] ZIENKIEWICZ O., TAYLOR R., ZHU J.: The finite element method: Its basis & fundamentals, August 2008. 12

[ZXS*12] ZHU L., XU W., SNYDER J., LIU Y., WANG G., GUO B.: Motion-guided mechanical toy modeling. *ACM Trans. Graph. 31*, 6 (2012), 127:1–127:10. 3

Appendix

A: Computation of $\mathbf{K}_{bend}$ for shell elements

Since we are using triangular shell elements, the shape functions used to elaborate strain-displacement relationship are based on barycentric coordinates. Let us denote the 2D coordinates of triangle vertices, i, j, k, by (x_i, y_i), (x_j, y_j) and (x_k, y_k) respectively (see Fig. 3), then the barycentric coordinate L_i for vertex i can be determined by the following equation [Log11]:

$$L_i = \frac{a_i + b_i x + c_i y}{2\Delta},$$
$$a_i = x_j y_k - x_k y_j, b_i = y_j - y_k, c_i = x_k - x_j, \quad (14)$$
$$\Delta = \frac{b_i c_j - b_j c_i}{2}.$$

L_j,L_k are computed similar to Eq. 14 using i, j, k as positive cyclic permutation.

The bending behavior of a triangular shell element can be determined by $\{w, \theta_x, \theta_y\}$ at its three vertices respectively. While deriving the shape functions, one needs to guarantee that the relationship between w and θ_x in Eq. 2 are imposed. In a nutshell, the shape function $\mathbf{N}$ can be described by a 1×9 vector which is multiplied to the 9 bending DOFs defined at the thee triangle vertices to form the interpolation function of the vertical displacement w:

$$\mathbf{N}^T = \begin{bmatrix} P_1 - P_4 + P_6 + 2(P_7 - P_9) \\ -b_j(P_9 - P_6) - b_k P_7 \\ -c_j(P_9 - P_6) - c_k P_7 \\ P_2 - P_5 + P_4 + 2(P_8 - P_7) \\ -b_k(P_7 - P_4) - b_i P_8 \\ -c_k(P_7 - P_4) - c_i P_8 \\ P_3 - P_6 + P_5 + 2(P_9 - P8) \\ -b_i(P_8 - P_5) - b_j P_9 \\ -c_i(P_8 - P_5) - c_j P_9 \end{bmatrix}, \quad (15)$$

where $P = [P_1, P_2, P_3, P_4, P_5, P_6, P_7, P_8, P_9]$ is

$$P_1 = L_i,\ P_2 = L_j,\ P_3 = L_k,\ P_4 = L_i L_j,\ P_5 = L_j L_k,\ P_6 = L_k L_i,$$
$$P_7 = L_i^2 L_j + \frac{1}{2} L_i L_j L_k (3(1-\mu_k)L_i - (1+3\mu_k)L_j + (1+3\mu_k)L_k),$$
$$P_8 = L_j^2 L_k + \frac{1}{2} L_i L_j L_k (3(1-\mu_i)L_j - (1+3\mu_i)L_k + (1+3\mu_i)L_i),$$
$$P_9 = L_i^2 L_j + \frac{1}{2} L_i L_j L_k (3(1-\mu_k)L_k - (1+3\mu_k)L_i + (1+3\mu_k)L_j), \quad (16)$$

where:

$$\mu_i = \frac{l_k^2 - l_j^2}{l_i^2}, \quad (17)$$

μ_j,μ_k are computed similar to Eq. 14, using i, j, k as positive cyclic permutation. l_i, l_j, l_k are the length of opposite edge of i, j, k in a triangle. Using virtual work theory, the element stiffness matrix $\mathbf{K}_{bend}$ is derived as:

$$\mathbf{K}_{bend} = \iiint \mathbf{B}_b^T \mathbf{D}_b \mathbf{B}_b \mathrm{dxdydz}, \quad (18)$$

where $\mathbf{D}_b$ is a matrix to represent material properties, and $\mathbf{B}_b$ is a strain-displacement matrix to convert the displacement variables into Cauchy strain in linear elasticity, where $\mathbf{B}_b$ in the case of Kirchhoff plate bending is calculated by:

$$\mathbf{B}_b = (\mathbf{L}\nabla)\mathbf{N}. \quad (19)$$

We expand Eq. 19:

$$\mathbf{B}_b = \begin{bmatrix} \frac{\partial}{\partial x}, 0 \\ 0, \frac{\partial}{\partial y} \\ \frac{\partial}{\partial y}, \frac{\partial}{\partial x} \end{bmatrix} \begin{bmatrix} \frac{\partial}{\partial x} \\ \frac{\partial}{\partial y} \end{bmatrix} \mathbf{N} = \begin{bmatrix} \frac{\partial^2}{\partial x^2} \\ \frac{\partial^2}{\partial y^2} \\ 2\frac{\partial^2}{\partial x \partial y} \end{bmatrix} \mathbf{N}. \quad (20)$$

B: Computation of $\frac{\partial \mathbf{K}_{ele}}{\partial t}$ for shell elements

The computation of the closed-form derivative of the stiffness matrix to thickness parameters is performed in two stages: (1) compute the derivative for each element stiffness matrix; (2) sum the derivatives at corresponding entries in the global stiffness matrix to obtain a polynomial representation of the derivatives used in sensitivity analysis.

Suppose that a shell triangle is extruded with a thickness parameter t. For the stretch deformation part for a shell, we have [ZTZ08]:

$$\mathbf{D}_s = \frac{E}{1-\nu^2} \begin{bmatrix} 1 & \nu & 0 \\ \nu & 1 & 0 \\ 0 & 0 & \frac{(1-\nu)}{2} \end{bmatrix}, \quad (21)$$

$$\mathbf{B}_s = \begin{bmatrix} \frac{\partial N_1}{\partial x} & 0 & .. & \frac{\partial N_3}{\partial x} & 0 \\ 0 & \frac{\partial N_1}{\partial y} & .. & 0 & \frac{\partial N_3}{\partial y} \\ \frac{\partial N_1}{\partial y} & \frac{\partial N_1}{\partial x} & .. & \frac{\partial N_3}{\partial x} & \frac{\partial N_3}{\partial y} \end{bmatrix}, \quad (22)$$

where N_1, N_2 and N_3 are the linear shape functions at three triangle vertices. For stretch part, we have:

$$\mathbf{K}_{stre} = \iint \mathbf{B}_s^T \mathbf{D}_s \mathbf{B}_s t \, dx \, dy. \quad (23)$$

Therefore, the derivative to thickness parameter t is:

$$\frac{\partial \mathbf{K}_{stre}}{\partial t} = \iint \mathbf{B}_s^T \mathbf{D}_s \mathbf{B}_s \, dx \, dy. \quad (24)$$

For the plate bending part, the matrix $\mathbf{D}_b$ in Eq. 18 is:

$$\mathbf{D}_b = \frac{Et^3}{12(1-\nu^2)} \begin{bmatrix} 1 & \nu & 0 \\ \nu & 1 & 0 \\ 0 & 0 & \frac{(1-\nu)}{2} \end{bmatrix}, \quad (25)$$

Since the matrix $\mathbf{B}_b$ in Eq. 18 in plate bending is calculated on the mid-surface and does not relate to t, we can compute the derivative of $\mathbf{K}_{bend}$ to t as:

$$\frac{\partial \mathbf{K}_{bend}}{\partial t} = \iint \mathbf{B}_b^T \frac{\partial \mathbf{D}_b}{\partial t} \mathbf{B}_b \, dx \, dy. \quad (26)$$